Cross-flow aerodynamics of bridge cables with wire meshes

Matejicka, Lubomir; Koss, Holger H.; Georgakis, Christos T.

Published in:
Journal of Wind Engineering and Industrial Aerodynamics

Link to article, DOI:
10.1016/j.jweia.2022.104941

Publication date:
2022

Document Version
Publisher's PDF, also known as Version of record

Journal of Wind Engineering & Industrial Aerodynamics 223 (2022) 104941

Contents lists available at ScienceDirect

Journal of Wind Engineering & Industrial Aerodynamics

journal homepage: www.elsevier.com/locate/jweia

Cross-flow aerodynamics of bridge cables with wire meshes

Lubomir Matejicka [a,*], Holger H. Koss [b], Christos T. Georgakis [a]

[a] Department of Civil and Architectural Engineering, Aarhus University, Inge Lehmanns Gade 10, 8000 Aarhus, Denmark
[b] Department of Civil Engineering, Technical University of Denmark, Brovej 118, 2800 Kgs. Lyngby, Denmark

ARTICLE INFO

Keywords:
Wind tunnel testing
Force coefficients
Den Hartog galloping
Vortex shedding
Flow visualisation

ABSTRACT

Adverse weather conditions in the northern regions during winter might lead to accumulation of ice or snow on bridge cables and consequently trigger ice shedding. The falling ice poses a risk for the traffic and pedestrians below, which often results in bridge closures and/or insurance claims. A passive surface-modifying device in the form of a steel wire mesh tautened on the surface of a cable sheath was previously found to substantially reduce the risk associated with falling ice through improved ice retention. In this paper, the cross-flow aerodynamic behaviour of bridge cables fitted with steel wire meshes is investigated in detail. The wire mesh generally resulted in higher levels of aerodynamic drag when compared with a plain cable sheath, although the Reynolds number dependence was highly reduced. Several angles of attack were investigated and no instability issues with respect to the across-wind vibrations were observed for any of the tested wire mesh configurations based on the quasi-steady theory. Even though vortex shedding was still present in all cases, the intensity of the fluctuating lift forces was much lower than that of the plain cable. To investigate basic aspects of the flow structure produced by the wire mesh, two flow visualisation techniques, combined with streamwise wind speed measurements in the near wake, were further used and are discussed.

1. Introduction

The growing popularity of cable-supported bridges around the world has highlighted the problem of atmospheric icing of bridge cables in recent years. A combination of specific atmospheric conditions at many bridge locations in colder regions may lead to precipitation icing in the form of freezing rain or wet snow. Prolonged exposure of bridge cables to these conditions can result in accretions with a thickness of up to several centimetres. Once accreted, the strong adhesive bond between the ice and the cable surface can persist for hours or even days in favourable weather conditions, typically with temperatures below freezing (Nims et al., 2014). However, when the sky clears up and the solar radiation transmitted through the ice heats up the surface of the cable or when the air temperature rises above zero, this bond is significantly weakened. At the same time, the cohesion of the accreted ice diminishes. Eventually, the combined effect of wind and gravity overcomes the residual adhesive and cohesive forces and the ice accretions start to break and slip off the cables. Sizeable fragments of ice or snow consequently fall down on the bridge deck and endanger the bridge users. Despite the ongoing research and a number of potential countermeasures, bridge closures are currently the only reliable way to prevent injuries and damage to the traversing traffic. As the closures last from a few hours up to several days, the ensuing traffic jams and delays can have a negative impact on the regional economy. In addition, such incidents often lead to public inquiries and investigations by local authorities.

Aside from the anti-icing or de-icing performance, many of the proposed ice prevention and removal systems for bridge cables face issues with installation and maintenance costs. One of the possible solutions to improve the cost-effectiveness is the application of passive systems based on cable surface modifications. Previous investigations (Matejicka et al., 2019) showed that the enhanced ice retention capability of a cable surface with concave fillets can substantially reduce the risk of ice shedding. As opposed to the conventional cable surface with helical fillets, enhanced ice retention of the concave-filleted surface leads to prolonged melting and fragmentation of the accreted ice into smaller pieces. Furthermore, the aerodynamic performance of the concave-filleted cable surface was shown to match or even outperform the conventional cable surfaces in terms of drag and aerodynamic stability (Kleissl, 2013; Burlina et al., 2018). Being an integral part of the cable sheath, the concave-filleted surface mostly represents a viable option for new cable-supported bridges. To provide a readily available retrofit solution with the ice retention capability for bridges in operation, a new cable surface fitted with a steel wire mesh was proposed. Although the preliminary ice shedding tests indicated improved ice retention performance, the wind tunnel tests also revealed

* Corresponding author.
E-mail addresses: lu.matejicka@protonmail.com (L. Matejicka), hko@byg.dtu.dk (H.H. Koss), cg@cae.au.dk (C.T. Georgakis).

https://doi.org/10.1016/j.jweia.2022.104941
Received 9 November 2021; Received in revised form 10 February 2022; Accepted 15 February 2022
Available online 27 February 2022

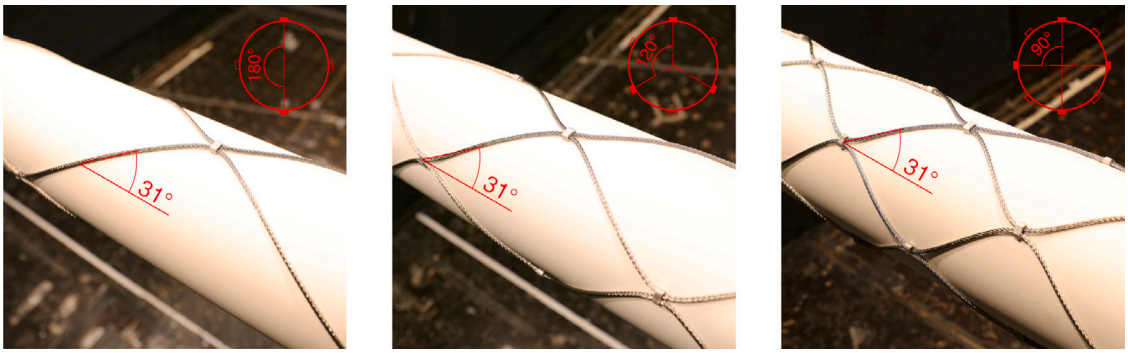

Fig. 1. Wire mesh configurations: IRWM 4 × 4 mm (left), IRWM 6 × 4 mm (centre) and IRWM 8 × 4 mm (right).

increased values of drag for these surfaces (Matejicka et al., 2021). As a sufficiently low drag coefficient of cable sheaths is one of the main design criteria for cable-supported bridges, the current study is aimed at elucidating the aerodynamic behaviour of cable sheaths fitted with wire meshes in dry conditions. This serves two purposes: to partially assess the aerodynamic performance of this cable surface modification for application in the industry; and to gain deeper understanding of the flow behaviour for potential optimisation of the wire mesh geometry. To achieve this, a detailed wind tunnel investigation of three different wire mesh configurations in cross-flow, i.e. the cable axis normal to the flow, was conducted. The investigation comprised static tests for the determination of force coefficients at multiple angles of attack, evaluation of Den Hartog's criterion for galloping instability, analysis of fluctuating lift forces, wake measurements, and flow visualisation of the cable surface and the near wake.

2. Experimental investigation

2.1. Cable sections

Four full-scale sections of high-density polyethylene (HDPE) tubing, commonly used as the outermost protection layer of stay cables, were tested. The tubing with a diameter D of 160 mm and a wall thickness of approximately 6.2 mm was produced by extrusion and provided by a stay cable manufacturer. The individual sections for the tests were cut to a length of 1.7 m. The first cable section was the original plain HDPE stay pipe, representing a well-known case of a circular cylinder and serving as a reference section.

The other three cable sections were fitted with interconnected steel wire ropes forming a mesh on their surface. Each wire rope had a diameter of 4 mm with a 7 × 7 construction (helical pattern of 7 strands composed of 7 wires). The wire ropes were alternately connected to the adjacent ones by 6 mm wide aluminium sleeves, essentially forming a mesh pattern with a helix angle of 31° (Fig. 1). Once the mesh was assembled, the ends of the wire ropes were threaded through holes in two anchor plates fixed at both ends of the cable. One end of the wire ropes was anchored with U-bolt clamps behind the anchor plate and the other end was clamped to a temporary anchor plate. This plate was free to slide along the cable axis on threaded bars with nuts connected to the permanent anchor plate. The wire mesh was then tensioned by tightening the nuts against the temporary anchor plate until the final mesh geometry was reached and no slack in the wire ropes was present. Subsequently, U-bolt clamps were used to secure the stressing side of the wire ropes to the permanent anchor plate. The three wire mesh configurations consisted of 4, 6, and 8 wires and are referred to as IRWM 4 × 4 mm, IRWM 6 × 4 mm, and IRWM 8 × 4 mm respectively, where IRWM stands for Ice Retention Wire Mesh.

2.2. Wind tunnel facility

The experimental investigation was conducted in the closed-circuit Climatic Wind Tunnel at Force Technology in Kgs. Lyngby, Denmark. The wind tunnel has a test section of 2 m by 2 m with a length of 5 m. The maximum wind speed is approximately 31 m/s and the free-stream turbulence intensity is in the range of 0.4 to 0.6%. Further design specifications of this wind tunnel are outlined in Georgakis et al. (2009).

2.3. Experimental setup

2.3.1. Static setup

The tolerances of the extrusion process of thermoplastic materials as well as the storage and handling of stay pipes induce inherent deviations from a perfect circular and straight shape of the pipes. For this reason, the stay pipe sections were fitted on a smaller aluminium cylinder with eight equidistant longitudinal rails to minimise these deviations and to increase their bending stiffness. At the same time, the aluminium cylinder created a solid connection with the rest of the test rig, ensuring a direct force transfer. As discussed above, an anchor plate was mounted on each side of the cylinder for the tensioning and anchoring of the wire ropes. The assembled cable sections were then mounted horizontally in the centre of the test section between the wind tunnel walls (Fig. 2). The supporting parts of the cylinder were further extended through the wind tunnel walls, where they were connected to two 6-DoF force sensors (AMTI MC3A-500) via flexible joints and fixed to the rigid frame of the wind tunnel. To minimise flow distortion at the cable ends and to ensure a nearly two-dimensional flow, two circular end plates with a diameter of 1 m and a thickness of 9 mm were used. The edges of the end plates were 1 mm thick and had an 8° bevel towards the wind tunnel walls to reduce the level of turbulence around them. The distance between the end plates was 1.6 m and constituted the effective length L for force measurements, resulting in a cable aspect ratio of 10. The remaining part of the 1.7 m cable section extended through the end plates on both sides to exclude the anchoring area from the flow. This required the end plate openings to be of larger diameter than the tested cable sections to avoid any interference between the cable model and the end plates. However, as found by Keefe (1962), having unsealed gaps between the end plates and the cable model reduces the magnitude of fluctuating forces and the correlation length of vortex shedding in the subcritical flow regime. To mitigate this effect, duct tape was used to seal the gaps, leaving a clearance of approximately 0.3–0.6% of the cylinder diameter. As shown in the results section, this was found sufficient to obtain the expected magnitude of the fluctuating lift forces (Fig. 9a). The static setup was thereafter finalised by covering the supporting parts of the rig between the walls and the end plates with circular dummy sections with a diameter of 220 mm.

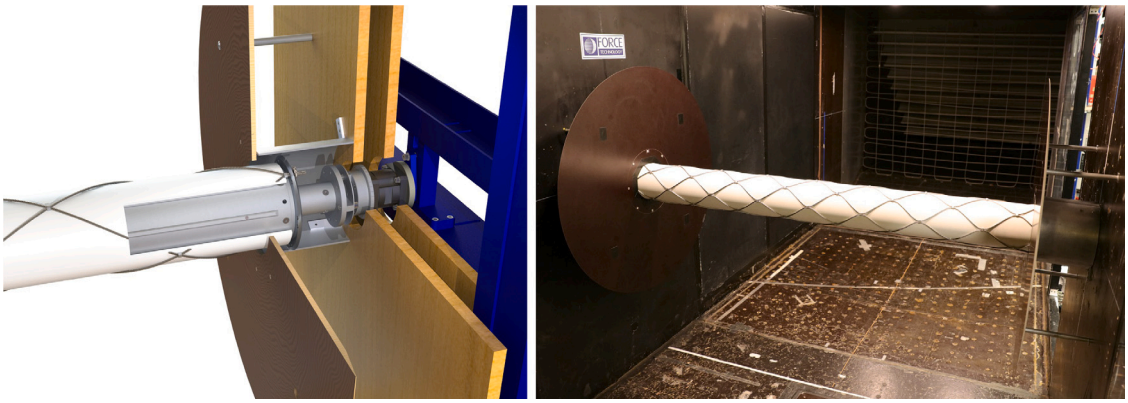

Fig. 2. Static setup: detail of the end connection (left), upstream view inside the wind tunnel (right; duct tape sealing is visible at the left cable end).

2.3.2. Wake measurements

Following the analysis of Aydin et al. (2014), the quasi-two-dimensionality of the flow was verified by streamwise wind speed measurements in the near wake of the plain cable section. A TFI Cobra Probe attached to a wing profile was placed at a distance of $4.3D$ downstream and $2.5D$ transversely from the cable axis at three different positions in the spanwise direction (Fig. 3a). The first lateral position was located at the cable midspan and the other two were positioned symmetrically $2.5D$ from it. The measurements were taken at four different wind speeds, corresponding to the Reynolds number Re range of approximately 0.4–3.1 $\times$ 10^5. The obtained signals were subsequently analysed and compared in the frequency domain in terms of the Strouhal number St and the spectral density S_{xx} normalised by the maximum spectral ordinate $S_{xx,max}$. Fig. 4 shows matching spectral peaks for the first three Reynolds number values, which corresponds to the occurrence of regular vortex shedding in the subcritical regime. These results generally demonstrate the absence of a spanwise variation in the vortex shedding frequency and hence indicate the suitability of the employed setup to produce a near-two-dimensional flow. At $Re \approx 3.1\times10^5$, the flow was in the transition to the supercritical regime, characteristic for low values of drag and a narrow wake. Due to the reduced width of the wake, the probe was largely in the free stream outside the wake and no distinct narrow-band peak associated with vortex shedding could be identified. Nevertheless, certain variations in the spectral curves caused by the proximity to the wake were observed for all three positions.

Moreover, further wind speed measurements with the TFI Cobra Probe in the near wake were carried out for the three cable sections with wire meshes. As in the previous case, the Cobra Probe was positioned $4.3D$ downstream of the cable axis. Based on the smoke flow visualisation, the vertical distance z/D from the horizontal cable plane was set to $1.375D$, $1.688D$ and $2D$ to capture the wind speed fluctuations caused by vortex shedding. Additionally, another location in the wake centreline at $0D$ was added. In the lateral direction parallel to the cable axis, the probe was placed in two positions corresponding to the spanwise locations of two neighbouring wire mesh nodes. This was done to investigate the influence of the varying cross section on the spanwise correlation of the flow in the wake. The first position was at the midspan, above the central node in the top position, and the second spanwise position was aligned with the neighbouring set of nodes as shown in Fig. 3b. Since there were three different wire mesh configurations, the distance between the neighbouring sets of nodes varied and the second position of the Cobra Probe was adjusted accordingly.

2.3.3. Flow visualisation

Flow visualisation of the near wake of the cable sections was based on the illumination of smoke particles in the flow. For these tests, a water-based smoke generator with a maximum smoke output of 720 m^3/min and a particle size of 0.2–0.3 μm was used together with a 532 nm continuous wave diode-pumped solid state laser. To create a laser sheet illuminating the whole width of the cable wake, a Powell lens with a 45° fan angle was installed on the laser. The resulting thickness of the laser sheet was around 2 mm. The smoke was injected into the flow approximately 0.5 m upstream of the cable via a hose and an injection tube connected to a vertical wing profile with slots in the trailing edge. The laser was placed approximately 2.5 m downstream of the cable and set to illuminate the central vertical plane normal to the cable axis (Fig. 5).

Additionally, surface flow visualisation utilising oil paint was performed to supplement the near-wake smoke visualisation. The applied oil paint solution was a mixture of linseed and diesel oil with carbon dust acting as a colour pigment (Fig. 12).

2.4. Test methods

2.4.1. Static tests

All force measurements were sampled at a frequency of 2048 Hz for a period of 30 s and converted to the corresponding time-averaged along-wind (drag) and across-wind (lift) forces. These forces were measured at wind speeds ranging from approximately 6 to 31 m/s in 1 m/s increments. To control the wind speed, a pitot tube located approximately 2 m upstream and connected to a differential pressure transmitter was used. Whilst the pressure difference and the air temperature were sampled simultaneously with the forces, the barometric pressure and relative humidity were recorded from their corresponding sensors manually. The force coefficients C_D and C_L were then calculated as:

$$C_D = \frac{F_D}{0.5\rho\bar{U}^2LD} \tag{1}$$

$$C_L = \frac{F_L}{0.5\rho\bar{U}^2LD} \tag{2}$$

where F_D and F_L are the mean along-wind and across-wind forces, $\bar{U}$ is the mean wind speed, L is the effective length of the cylinder, D is the diameter of the plain cable sheath, and ρ is the air density. The size of the cable sections relative to the cross-sectional area of the test section resulted in a blockage ratio of 8%. Therefore, the drag coefficients were corrected for blockage according to the Maskell III method described by Cooper et al. (1999).

The cable sections were tested at multiple angles of attack α, i.e. rotation around the cable axis. Whilst the reference plain cable sheath was tested at 12 different angles with 30° increments, the cable sections with wire meshes were rotated by smaller 10° increments in a 0–90° range. In the case of wire meshes, the starting position, denoted as 0°, was defined with a set of connection nodes parallel to the cable axis being at the top of the cable section. The purpose of varying the angle of attack was to investigate its effect on the force coefficients and to

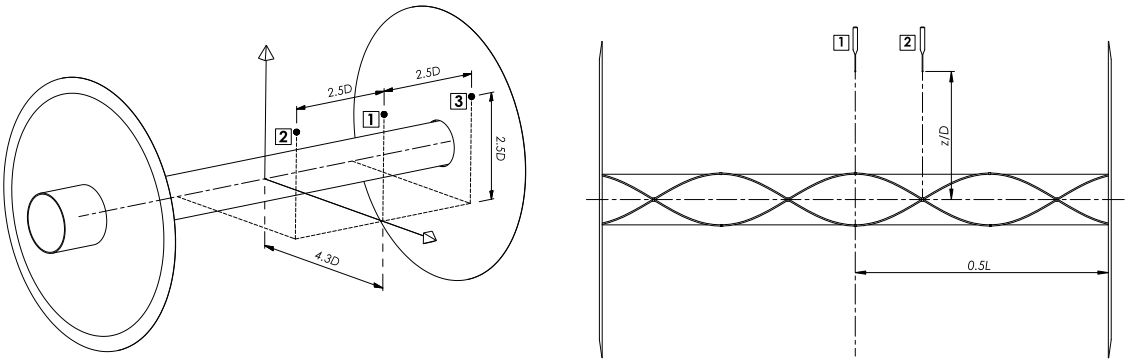

Fig. 3. Position of the TFI Cobra Probe for wake measurements: plain cable section (left), wire mesh cable sections (right; example of IRWM 4 × 4 mm).

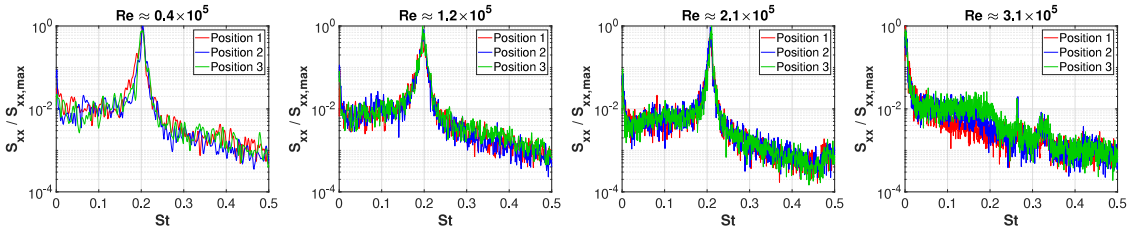

Fig. 4. Spectral densities of the near-wake wind speed fluctuations for three different spanwise locations.

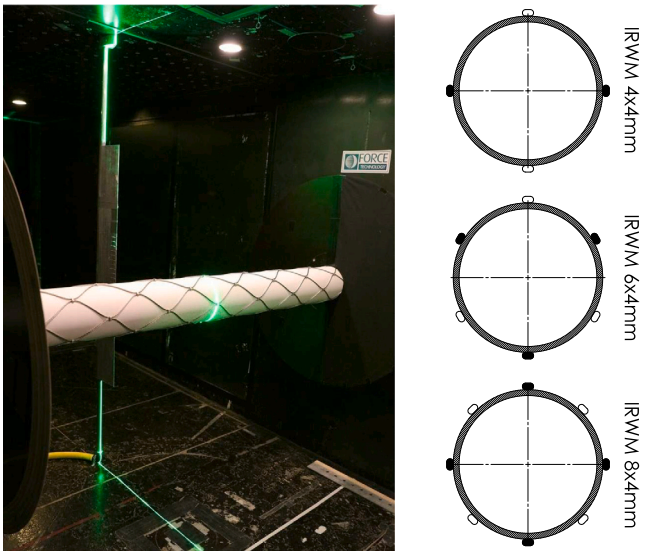

Fig. 5. Test setup for smoke flow visualisation (left) and illuminated cross sections (right).

evaluate the quasi-steady aerodynamic damping for Den Hartog galloping instability. This was expressed in the form of a nondimensional parameter according to Macdonald and Larose (2006) as:

$$Z_a = \frac{Re}{8\pi}\left(C_D + \frac{\partial C_L}{\partial \alpha}\right) \tag{3}$$

The time histories of the unsteady lift forces were further analysed in the frequency domain to investigate the occurrence of the vortex shedding phenomenon and possible Reynolds number effects. Since the test setup employed in this study was based on direct force measurements, only the fluctuations of the total lift forces could be analysed. The power spectral density of the lift force signal was estimated by using the Welch's method. The frequency of vortex shedding f_s was thereafter obtained for each wind speed and angle of attack to calculate the dimensionless Strouhal number defined as:

$$St = \frac{f_s D}{\bar{U}} \tag{4}$$

Additionally, to compare the intensity of the fluctuating lift between individual cable sections across the full tested Re range, the total RMS (Root Mean Square) lift coefficients were calculated as:

$$C_{L'} = \frac{F_{L'}}{0.5\rho\bar{U}^2 LD} \tag{5}$$

2.4.2. Wake measurements

At each Cobra Probe position, four measurements at wind speeds corresponding to $Re \approx 0.4\times10^5$, 1.2×10^5, 2.1×10^5 and 3.1×10^5 were taken. The Cobra Probe signal was sampled for a period of 60 s at a frequency of 2048 Hz. As in the case of fluctuating lift forces, the signals were analysed in the frequency domain by employing the Welch's method to obtain the power spectral density estimate. The spectral density was thereafter normalised with respect to the frequency and the geometrical variance of the spectrum. To facilitate the evaluation and comparison of the vortex shedding frequency with the force measurements, the frequency scale was converted to the nondimensional Strouhal number.

The signals were also analysed in the time domain to evaluate the streamwise turbulence intensity in the near wake. The turbulence intensities at the given locations were used to obtain an approximate comparison of the near wake width and spanwise variation at the four wind speeds. The turbulence intensity was defined as the ratio of the standard deviation of the streamwise wind speed σ_u and the mean streamwise wind speed $\bar{U}$:

$$I_u = \frac{\sigma_u}{\bar{U}} \tag{6}$$

2.4.3. Flow visualisation

The smoke-based flow visualisation tests were performed at three different Reynolds numbers of approximately 0.4×10^5, 1.2×10^5 and 2.1×10^5. A camera placed outside the test section was set to capture the illuminated wake up to a distance of $9.4D$ from the leeward side of the cable section. Due to the quick-dispersing property of the smoke, the smoke output was adjusted accordingly with the increasing wind

speed. The cable sections with wire meshes were tested in their starting position at $\alpha = 0°$.

For the surface flow visualisation, the oil paint mixture was applied to the central portion of the cable sections and covered a length of approximately $0.5L$. These tests were conducted at a wind speed of approximately 20 m/s, which corresponded to $Re \approx 2.1 \times 10^5$. Once exposed to the flow, the oil paint was driven by the friction forces in the near flow field and formed patterns that reflected the flow structures at the surface of the cable model.

3. Results and discussion

3.1. Force coefficients

The time-averaged drag and lift coefficients as functions of the Reynolds number for each angle of attack are shown in Fig. 6. As previously observed, a non-uniform surface roughness and a deviation from a perfect circular shape of plain HDPE cable sheaths affect the onset of the critical flow regime and the force coefficient values (Matteoni and Georgakis, 2012). This was confirmed in the current study, where the asymmetric one-bubble regime TrBL1 (Zdravkovich, 1997), characteristic for a steady non-zero lift and a drop in the drag, was initiated in the range of $Re \approx 2.3 \times 10^5 - 2.8 \times 10^5$ for different angles of attack (Figs. 6a and b). Additionally, whilst the symmetric two-bubble regime TrBL2 was reached at almost every angle of attack, the supercritical regime TrBL3 was attained in two cases only, further demonstrating the sensitivity of the flow in the critical region. The minimum drag coefficient measured in this flow regime was $C_D = 0.32$.

Contrary to the plain cable sheath, the cable sections with wire meshes experienced a rather limited Reynolds number dependence as well as an angle of attack dependence with some exceptions. The latter was caused by the rotational asymmetry of these cable sections about the central horizontal plane defined by the cable axis and the flow vector normal to it. Since the starting position at $\alpha = 0°$ was based on the mesh nodes at the topmost position, only IRWM 4 × 4 mm and IRWM 8 × 4 mm were considered symmetrical with respect to this plane at their 0° and 90° positions. IRWM 6 × 4 mm reached this symmetry first at $\alpha = 30°$ and again at $\alpha = 90°$. It should be noted that any discrepancies between the force coefficient curves of two mutually symmetrical cable positions were most likely the result of geometrical irregularities caused by the manual construction of the mesh.

The most prominent dependence of the drag coefficient on the Reynolds number was found for two pairs of angles of attack - α = 30°, 60° and α = 40°, 50°- in the case of IRWM 4 × 4 mm (Fig. 6c). These angles of attack constituted pairs of mutually symmetrical rotational positions with respect to the oncoming flow and therefore had approximately the same values of drag and opposite values of lift. The symmetry is also discernible for the other angle-of-attack pairs. Particularly, the lift coefficients at $\alpha = 20°$ and 70° behaved almost as a linear function of Re leading to higher values of lift at the maximum Re (Fig. 6d). However, when the cable section was at the starting 0° and equally symmetrical 90° positions, the lift coefficient remained near zero throughout the entire Re range. Furthermore, a minor Re dependence of the drag coefficient indicating a flow transition was observed in the lower Re range at these angles. At higher Re no dependence of the drag coefficient on Re was observed and the mean value of drag levelled of at $C_D = 0.9$.

A similar behaviour of the drag coefficient was observed for IRWM 6 × 4 mm. The initial drop of the drag coefficient was followed by a plateau established at $Re \approx 1.3 \times 10^5 - 1.8 \times 10^5$ with a mean value of C_D = 0.93 (Fig. 6e). Likewise, the lift coefficients showed a marginal Re dependence at lower Re and remained near zero throughout the tested Re range (Fig. 6f). The sole exception was a pair of mutually symmetrical angles of attack α = 40° and 80° with slightly higher values of the lift coefficient. Whilst the Re dependence was almost negligible at higher Re, the α dependence was more distinct, particularly for the drag coefficient. Above $Re = 2 \times 10^5$ the drag coefficient ranged from 0.86 $< C_D <$ 0.99.

IRWM 8 × 4 mm exhibited a limited Re and α dependence with the mean drag coefficient in the range of $1.1 < C_D < 1.15$ (Fig. 6g). The lift coefficient remained near zero and only minor variations were observed with respect to the angle of attack (Fig. 6h).

Despite the rotational asymmetry, the lift coefficients of all three wire mesh configurations remained close to zero with a few exceptions mentioned above. These results indicate that the drag of cable sections with the chosen wire mesh geometries increases with the number of wire ropes used, although there was a marginal difference between the meshes with 4 and 6 wire ropes. Moreover, the Re dependence seems to diminish with the growing number of wire ropes, similar to the increased surface roughness of a circular cylinder.

3.2. Aerodynamic damping

The evaluation of the aerodynamic damping based on Den Hartog's galloping instability criterion is presented in the form of a nondimensional parameter in Fig. 7. A transition to negative aerodynamic damping indicating a potential instability region is marked with a red dashed line. As shown in Fig. 7a, two areas of instability were identified for the plain cable section at different angles of attack in the critical flow regime. As discussed previously, surface and shape irregularities can affect the aerodynamic behaviour of a plain circular cylinder and therefore the areas of instability in Fig. 7a apply only to this specific cable section. Although these irregularities are unique for each HDPE sheath, these results show that negative aerodynamic damping in the critical flow regime can also occur for across-wind vibrations and not only for along-wind vibrations, i.e. the drag crisis (Macdonald and Larose, 2006). No instability was found for any of the cable sections with wire meshes. In all three cases, the aerodynamic damping showed a tendency to increase proportionally with growing Reynolds number (Figs. 7b, c and d). This was caused by a relatively low dependence of the force coefficients on the angle of attack and the Reynolds number.

3.3. Fluctuating lift forces

The analysis of the fluctuating lift forces of the plain cable section showed two discontinuous transitions of the Strouhal number in the critical flow regime (Fig. 8a) as previously described by Schewe (1983). Specifically, these jumps in St correspond to the TrBL1 and TrBL2 flow regimes, where the turbulent separation on one and then on both sides of the cylinder further downstream result in a narrower wake with a higher frequency of vortex shedding. The onset of the critical regime, marked by the distinct jump in St, varied for different α as already shown and discussed in the case of force coefficients. In the subcritical regime, the typical value of $St \approx 0.2$ with a very low scatter between individual angles of attack was observed.

All three wire mesh configurations exhibited vortex shedding with St being largely independent of Re for $Re > 1 \times 10^5$. The sole exception was found in the case of IRWM 4 × 4 mm for a pair of mutually symmetrical angles of attack at $\alpha = 30°$ and 60° (Fig. 8b). As suggested by their corresponding drag curves (Fig. 6c), a flow transition occurring in the range of $1 \times 10^5 < Re < 2 \times 10^5$ resulted in the decrease of St from 0.2 to 0.17. The mechanism behind this transition is, however, unknown at the moment. Additionally, a higher value of St of 0.2 was found for $\alpha = 40°$ and 50°, which similarly exhibited a pronounced drop in drag. The Strouhal number at the other angles of attack was approximately 0.16. A $St - \alpha$ dependence was further demonstrated by IRWM 6 × 4 mm with St ranging from approximately 0.17 to 0.2 at different α (Fig. 8c). This behaviour is closely correlated with that of the drag coefficient (Fig. 6e), where higher C_D values correspond to higher values of St. Lastly, the analysis of the fluctuating lift forces on IRWM 8 × 4 mm revealed St of approximately 0.2 with small variations at Re below 1×10^5 (Fig. 8d).

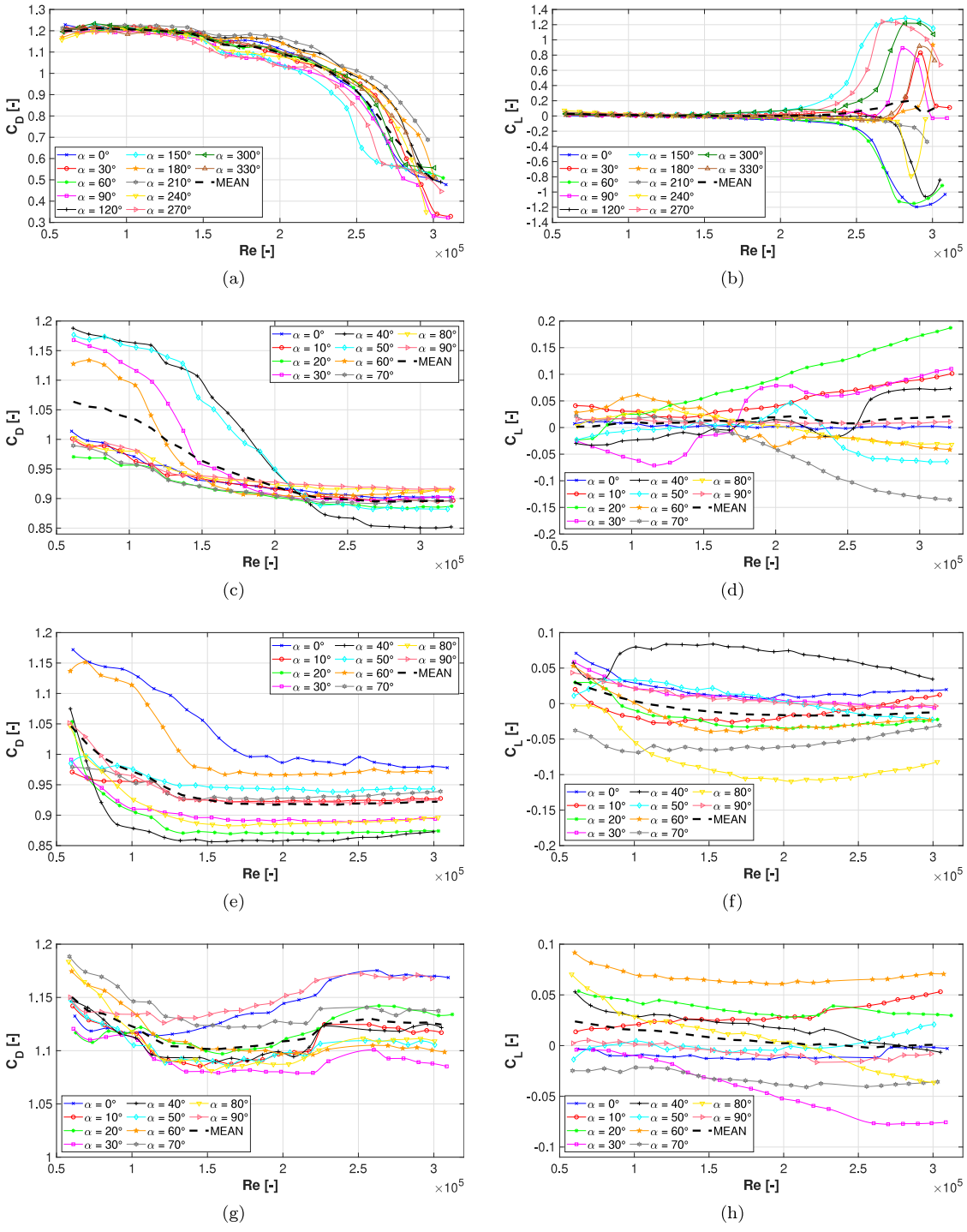

Fig. 6. Comparison of force coefficients: (a) Plain cable drag, (b) Plain cable lift, (c) IRWM 4 × 4 mm drag, (d) IRWM 4 × 4 mm lift, (e) IRWM 6 × 4 mm drag, (f) IRWM 6 × 4 mm lift, (g) IRWM 8 × 4 mm drag, (h) IRWM 8 × 4 mm lift.

The RMS lift coefficients are compared in Fig. 9. A common trend in all four cases is a progressive increase and a distant peak of $C_{L'}$ at higher Re. This was caused by the first natural frequency of the experimental rig coinciding with the frequency of vortex shedding, which led to a resonance affecting a broader range of Re. For this reason, a quantitative comparison between the individual cable sections can only be made at lower Re. Even though $C_{L'}$ based on the total lift fluctuations of the plain cable section cannot be directly compared with the sectional RMS lift coefficient of a circular cylinder commonly reported in the literature, a noticeable drop in $C_{L'}$ between the subcritical and supercritical regimes (Fig. 9a) agrees well with the results obtained by other authors (Schewe, 1983; Norberg, 2003). In comparison with the subcritical values of the plain cable section, all three wire mesh configurations exhibited lift fluctuations with a considerably lower intensity. The mean values of $C_{L'}$ in the region up to $Re = 1.5 \times 10^5$ were 0.47, 0.18, 0.12 and 0.27 for the plain cable section, IRWM 4 × 4 mm, IRWM 6 × 4 mm and IRWM 8 × 4 mm respectively. Similarly to the previous results, IRWM 4 × 4 mm displayed a strong angle-of-attack and Reynolds number dependence, which was evident for the α = 30°, 60° and α = 40°, 50° pairs (Fig. 9b). Minor α and Re effects were further observed in the case of IRWM 6 × 4 mm at α = 0° and 60°, which were symmetric with respect to the oncoming flow (Fig. 9c).

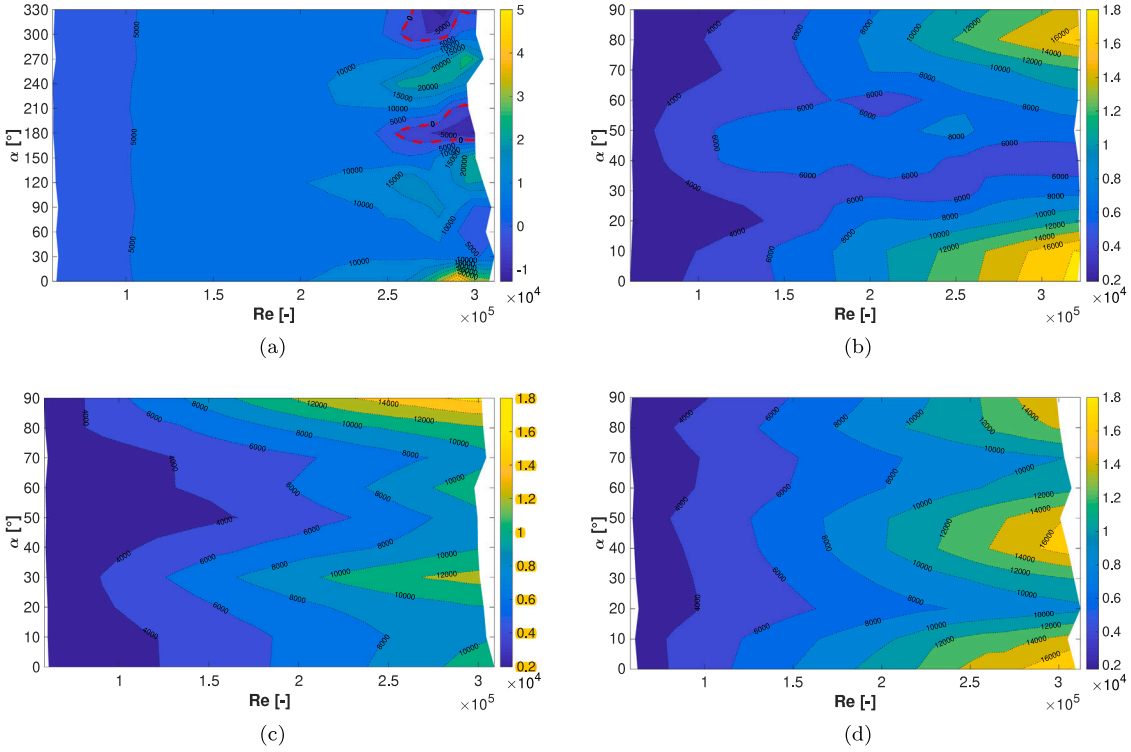

Fig. 7. Aerodynamic damping parameter Z_a: (a) Plain cable, (b) IRWM 4 × 4 mm, (c) IRWM 6 × 4 mm, (d) IRWM 8 × 4 mm. Note that due to the varying range of Z_a values, the colour bar limits of (a) differ from (b), (c) and (d). (For interpretation of the references to colour in this figure legend, the reader is referred to the web version of this article.)

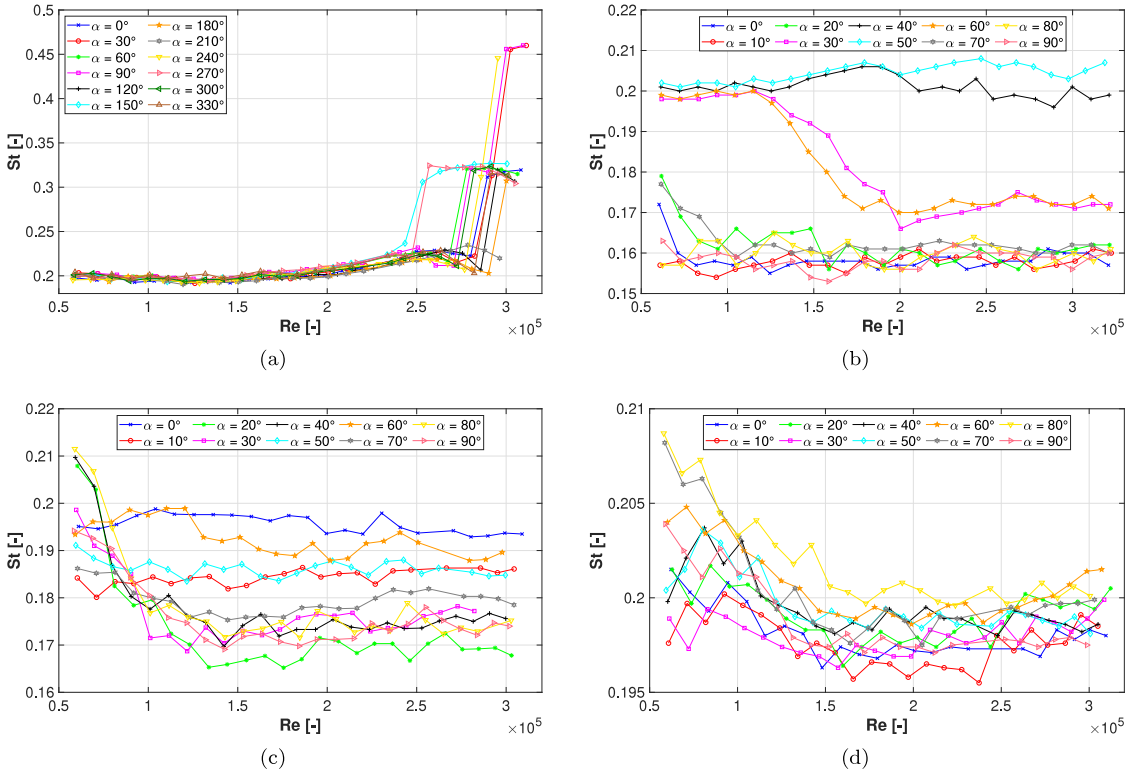

Fig. 8. Strouhal numbers: (a) Plain cable, (b) IRWM 4 × 4 mm, (c) IRWM 6 × 4 mm, (d) IRWM 8 × 4 mm.

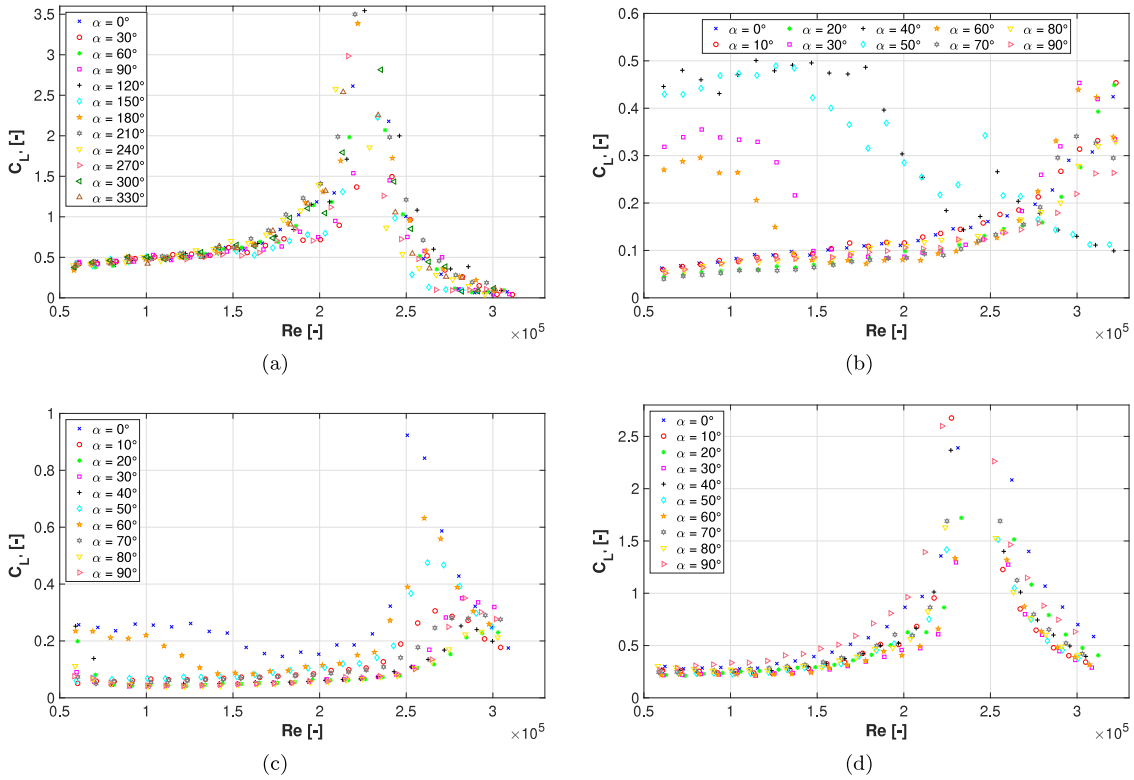

Fig. 9. RMS lift coefficients: (a) Plain cable, (b) IRWM 4 × 4 mm, (c) IRWM 6 × 4 mm, (d) IRWM 8 × 4 mm.

Contrarily, $C_{L'}$ of IRWM 8 × 4 mm was found to be relatively constant at each tested α in the lower Re range.

3.4. Wake measurements

The obtained power spectra of the streamwise wind speed measurements in the near wake of the three wire mesh configurations at different Reynolds numbers are presented in Fig. 10. In all cases, the individual spectra derived from wind speed measurements at two spanwise locations denoted as 'Position 1' and 'Position 2' were closely matched. The matching spectral peaks indicate a high degree of spanwise correlation of the time-averaged vortex shedding frequency and magnitude between a pair of neighbouring wire mesh nodes at different angular positions. However, due to the lack of simultaneous measurements at the two locations, the spanwise correlation of vortex shedding in the time domain could not be verified. Moreover, as the abscissa of the spectrum plots has a St scale, it can be seen that the values of St obtained from the wind speed (Fig. 10) and force measurements (Fig. 8) at $\alpha = 0°$ are in agreement. Similarly, the relative magnitude of the spectral peaks corresponds to the magnitude of $C_{L'}$ (Fig. 9) with IRWM 8 × 4 mm experiencing vortex shedding of higher intensity than IRWM 6 × 4 mm and IRWM 4 × 4 mm.

Fig. 11 provides a comparison of the streamwise turbulence intensity profiles of all four cable sections. The available data points show the turbulence intensity levels in the wake centreline and at three points near the free shear layer. For the wire mesh cable sections, turbulence intensity profiles at the two spanwise locations are available, whilst only the midspan profiles are provided for the plain cable section. It should be noted that many of the measurements in the wake centreline ($z/D = 0$) contained a significant number of out-of-range data points, i.e. points outside of the Cobra probe acceptance cone of ±45°. This was especially the case for IRWM 4 × 4 mm at $Re \approx 0.4{\times}10^5$, where the out-of-range data points amounted to 25% at Position 1 compared to 8% at Position 2. As the missing data points would lead to slightly higher values of the mean wind speed and lower values of the standard deviation, the real turbulence intensity levels in the wake centreline are expected to be marginally lower.

It is shown that the decrease in turbulence intensity at higher Re of the plain cable section (Fig. 11a) corresponds well with the narrowing of the wake and the drag reduction in the critical flow state. An agreement with the force coefficient results (Fig. 6) can also be seen from the turbulence intensity profiles of the three wire mesh configurations. As the variation of the drag coefficient with the Reynolds number of IRWM 4 × 4 mm and IRWM 8 × 4 mm at $\alpha = 0°$ was limited, the level of turbulence for different Re at the individual spanwise locations was very similar (Fig. 11b,d). An exception is the highest measured location at $z/D = 2$ for IRWM 4 × 4 mm, where the turbulence intensity at $Re \approx 0.4 \times 10^5$ was visibly higher. Although the force coefficients at this Re were not obtained, the corresponding power spectrum in Fig. 10 suggests a strong presence of vortex shedding with a distinct peak that might have caused the jump in turbulence intensity. In the case of IRWM 6 × 4 mm (Fig. 11c), the scatter of turbulence intensity at the nonzero positions z/D is highly correlated with the initial drop in drag followed by a plateau at $\alpha = 0°$ (Fig. 6e). Moreover, it was found that the difference in turbulence intensity levels between the two spanwise locations increased proportionally with the increased distance of neighbouring wire mesh nodes. Despite the spanwise correlation of vortex shedding demonstrated in Fig. 10, this indicates a higher degree of three-dimensionality of the flow for the wire mesh configurations with a smaller number of wire ropes.

3.5. Flow visualisation

The influence of the wire mesh on the airflow around the cable was further analysed through the use of flow visualisation. The alternating pattern formed by each of the tested wire mesh configurations affects the boundary-layer flow along the cable surface and the flow separation characteristics at the top and bottom of the cable cross-section. The flow features along the cable surface were revealed by oil paint

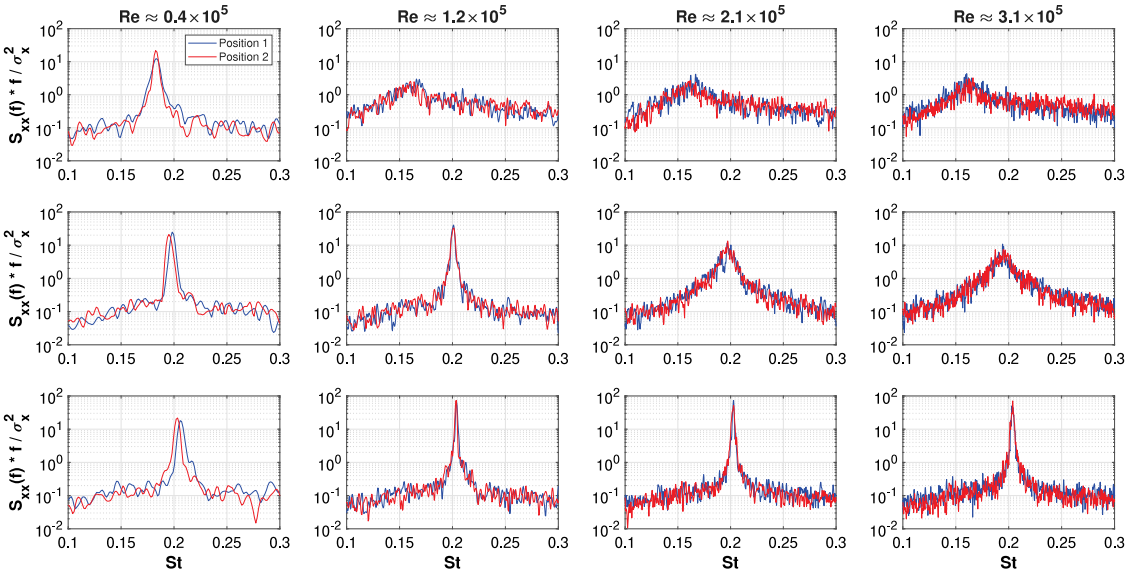

Fig. 10. Power spectra of streamwise wind speed measurements in the near wake: IRWM 4 × 4 mm (top), IRWM 6 × 4 mm (middle), IRWM 8 × 4 mm (bottom).

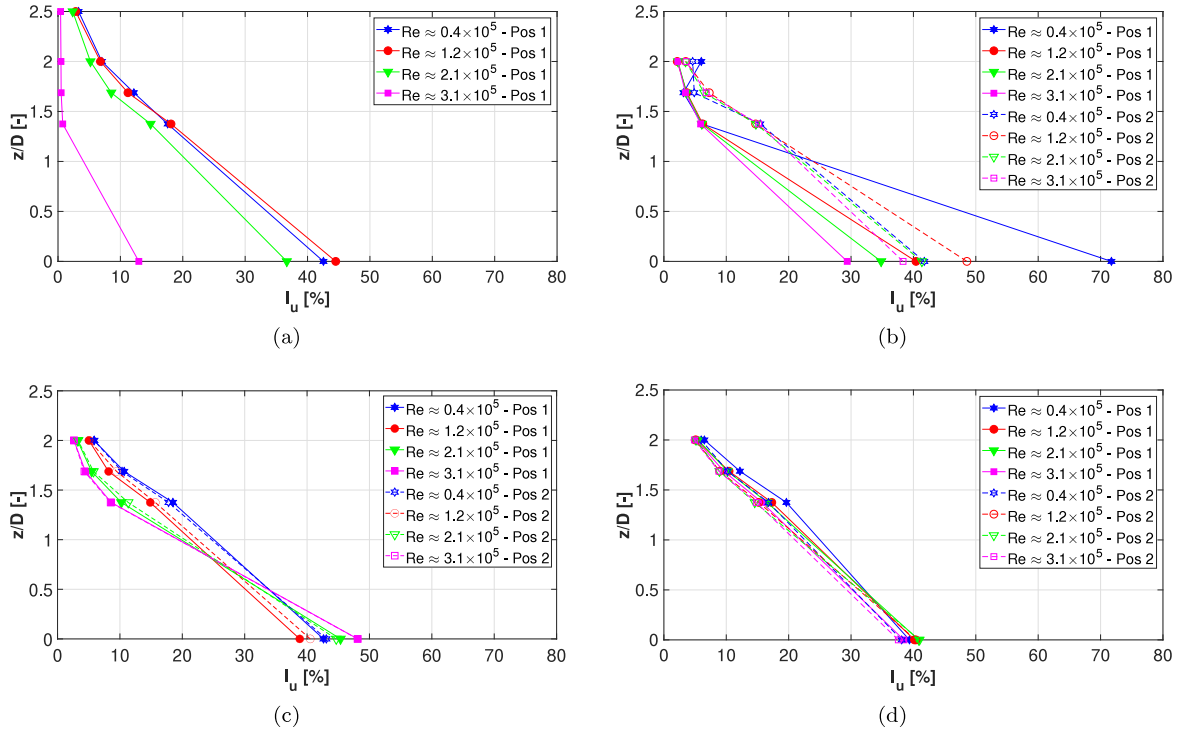

Fig. 11. Streamwise turbulence intensity profiles: (a) Plain cable, (b) IRWM 4 × 4 mm, (c) IRWM 6 × 4 mm, (d) IRWM 8 × 4 mm.

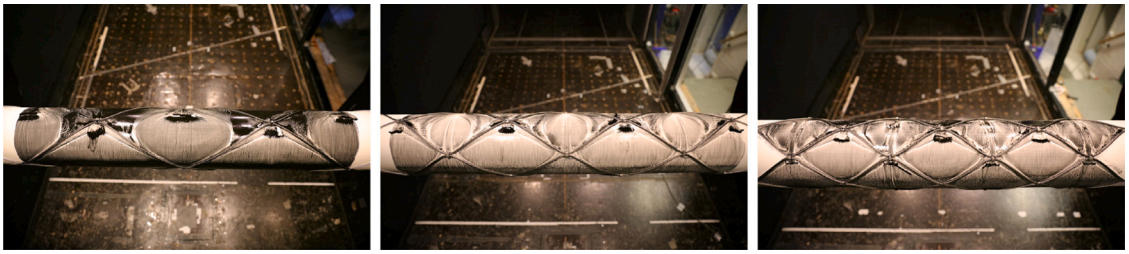

Fig. 12. Oil paint flow visualisation: IRWM 4 × 4 mm (left), IRWM 6 × 4 mm (centre) and IRWM 8 × 4 mm (right). (For interpretation of the references to colour in this figure legend, the reader is referred to the web version of this article.)

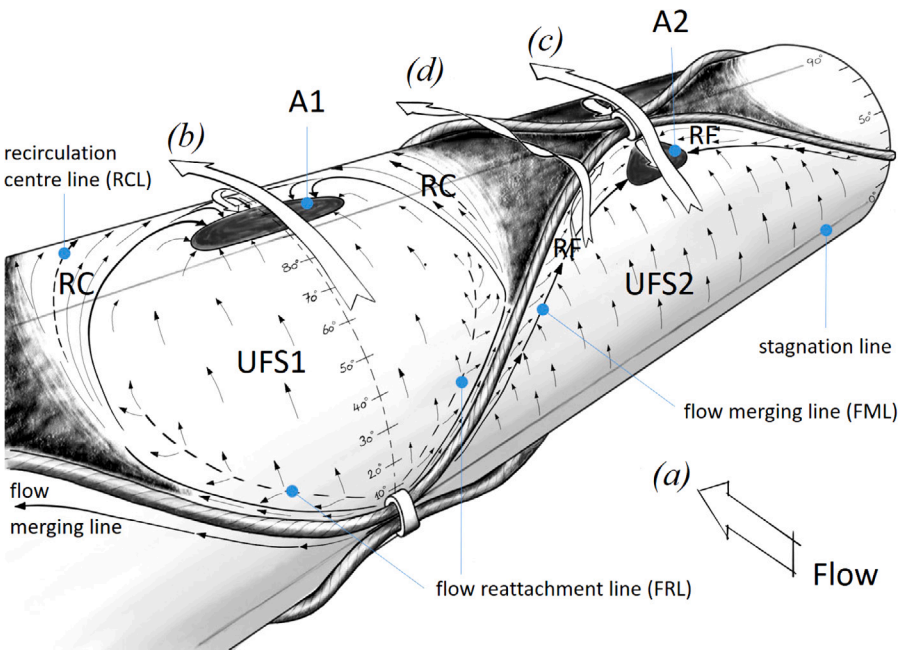

Fig. 13. Illustration of the shear flow along the cable surface from oil paint visualisation test on IRWM 4 × 4 mm.

visualisation as shown in Fig. 12 for a relative wind direction normal to the cable axis.

The diagonal wire rope orientation redirects or focuses the surface flow towards the aluminium connection sleeves. This effect is most pronounced on the upwind side of the cable but influences as well the flow on the rear part of the cable. The overall anatomy of this effect is illustrated in Fig. 13 on the example of IRWM 4 × 4 mm.

The approaching wind flow (a) divides into a flow along a largely undisturbed surface (b) and a flow dominated by the presence of the wire mesh (c) separating directly from the wire rope and the connection sleeve. The flow (b) over the undisturbed surface separates around the top of the cable section (~90°) forming a separation bubble behind the top indicated in position and size by the area A1. To this area of low surface shear, oil paint is driven by the dominating undisturbed flow shear (UFS1) on the upwind cable side and the recirculating flow (RC) on the cable rear side (see also Fig. 14) and accumulates here. A second accumulation zone, A2, is formed by the flow (c) in front of the connection sleeve. This zone reflects a 'focus point' of the undisturbed flow shear (UFS2) and the redirected flow (RF) in front of the wire rope, approaching from both sides to A2. The visualisation reveals the location where UFS2 and the flow redirected by the wire rope merge, creating a line of high surface shear (FML). Apart from flow redirection, the wire ropes lead to flow separation. Starting from the stagnation line, the flow separating from the wire rope reattaches again in the flow regime UFS1 along the flow reattachment line (FRL). Higher up, between 40° and 50°, the flow separating from the wire rope exhibits less reattachment and remains fully separated beyond 50° to 60° (d). This is reflected by the practically undisturbed oil paint surface between and behind the wire ropes. When compared with Fig. 11b, it can be seen that the undisturbed and reattached flow (b) generates much lower levels of turbulence in the near wake than the fully separated flow (c) passing the wire mesh node at the top.

Similar to the focusing effect on the upstream side of the cable sheath, the wire rope influences the surface flow on the rear side of the cable. As shown in Fig. 13, the undisturbed flow (b) separates from the cable surface behind the top of the cable cross-section forming a separation bubble reflected by the accumulation zone A1. The surface flow towards A1 on the cable rear side is enhanced by the wire mesh arrangement. As illustrated in Fig. 14, the flow recirculates over a significant area stretching as far as 140°. The zone of recirculating surface flow is indicated by the recirculation centre line (RCL), outside which the flow moving downwards is still influenced by the rear wire rope and gravity. This could lead to an enhancement or concentration of flow separation over the A1 area.

All surface flow features described above apply to all tested wire mesh configurations but change in size and magnitude with increasing mesh density.

Furthermore, the flow visualisation of the near wake revealed the presence of a Kármán vortex street for all four cable sections as already suggested by the results discussed above. Fig. 15 depicts the formation of alternating counter-rotating vortices over the midspan cross section at three different Reynolds numbers. Overall, only minor differences in the wake width are noticeable as the drag coefficient of all four cable sections varied minimally in the visualised Re range. In this case, the most apparent is the difference between IRWM 4 × 4 mm and IRWM 8 × 4 mm at $Re \approx 2.1 \times 10^5$ with $C_D = 1.0$ and 1.15 respectively.

Additionally, a distinct vortex street was observed in the turbulent wakes of the plain cable, IRWM 6 × 4 mm and IRWM 8 × 4 mm, whilst a slightly disorganised flow structure with a narrower wake was present in the case of IRWM 4 × 4 mm. This corresponds well with the lower RMS values of the fluctuating lift at $\alpha = 0°$ (Fig. 9b) and the lower values of the turbulence intensity at 'Position 1' (Fig. 11b) of IRWM 4 × 4 mm than those of the other cable sections. Nevertheless, the varying levels of turbulence intensity and the surface flow pattern observed between 'Position 1' (flow (b) in Fig. 13) and 'Position 2' (flow (c) in Fig. 13) suggest that the flow structure in the near wake produced by the flow (c) could be slightly different even though the vortex shedding frequency remains unchanged.

3.6. Overall assessment

The force coefficient results of the tested wire meshes revealed an increase in drag force of approximately 40%–70% when compared with conventional helically-filleted and pattern-indented cable surfaces (Kleissl and Georgakis, 2012). For the retrofitting of existing bridges, this would require an evaluation of the structural capacity of the pylons and foundations due to the increased horizontal load. In this regard, IRWM 4 × 4 mm performed the best with a mean C_D of 0.9. Although this might be considered a rather high value, this wire mesh geometry was also able to reduce the magnitude of vortex shedding

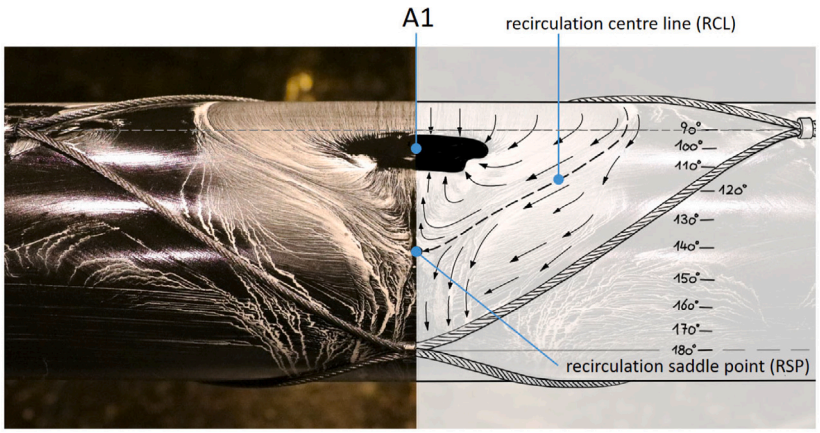

Fig. 14. Surface flow pattern on the rear side of IRWM 4 × 4 mm.

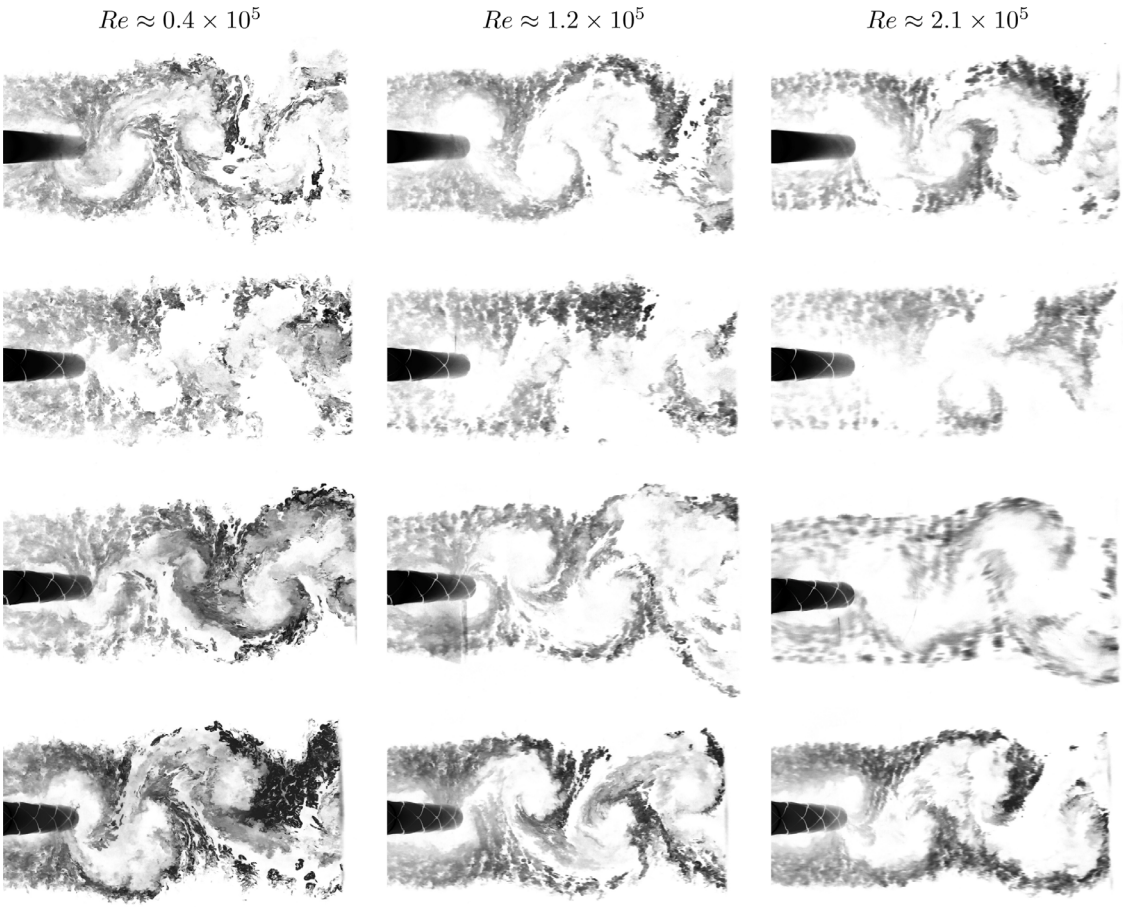

Fig. 15. Smoke flow visualisation, top to bottom: Plain cable, IRWM 4 × 4 mm, IRWM 6 × 4 mm and IRWM 8 × 4 mm.

significantly and despite the cross-sectional asymmetry at most angles of attack, no galloping instability was detected. Additionally, it is hypothesised that all three wire mesh configurations should be able to suppress the formation of water rivulets and therefore prevent the onset of rain–wind induced vibrations (RWIV). This could minimise the need for additional structural damping, however, dynamic wind tunnel tests are needed to further investigate their susceptibility to RWIV and other galloping-type vibrations. As the wire mesh geometries were chosen with respect to the practicality of their assembly and ice retention performance, the mesh pattern could be further optimised to reduce the level of drag based on the presented results.

4. Conclusions

A wind tunnel study of cable sections fitted with steel wire meshes designed to mitigate the risk of ice shedding was carried out. The static wind tunnel tests in cross-flow revealed a moderate dependence of the force coefficients on the Reynolds number and the angle of attack. This dependence was most apparent for IRWM 4 × 4 mm and IRWM

6 × 4 mm at several angles of attack in the lower Reynolds number range. The mean drag of the cable sections with wire mesh at the maximum wind speed was higher than that of the conventional cable surfaces, with drag coefficients of C_D = 0.9, 0.93, and 1.13 for wire meshes consisting of 4, 6 and 8 wire ropes, respectively. Despite the dependence, the mean lift coefficients were generally near zero and no instability was observed when evaluating the Den Hartog criterion for galloping occurrence. Furthermore, the analysis of fluctuating lift forces showed that all three wire mesh configurations exhibited vortex shedding across the full tested wind speed range, with Strouhal numbers equal or lower than those of the plain cable. Nevertheless, the magnitude of vortex shedding was much lower in the case of IRWM 4 × 4 mm and IRWM 6 × 4 mm as shown by the analysis of RMS lift coefficients and near-wake wind speed measurements. The presence of a von Kármán vortex street for all three cable sections fitted with wire meshes was additionally confirmed by the smoke flow visualisation of the near wake. Finally, the oil paint visualisation revealed various flow patterns along the surface of the wire mesh cable sections, which could be partially correlated with the differences in turbulence intensity in the near wake.

With respect to the density of the mesh pattern, the obtained results generally suggest that reducing the number of wire ropes can reduce the aerodynamic drag and the magnitude of the fluctuating lift, whilst increasing the angle-of-attack dependence and the spanwise variation of the flow in the near wake.

CRediT authorship contribution statement

Lubomir Matejicka: Conceptualisation, Data curation, Formal analysis, Funding acquisition, Investigation, Methodology, Visualisation, Writing – original draft. **Holger H. Koss:** Formal analysis, Resources, Visualisation, Writing – original draft. **Christos T. Georgakis:** Conceptualisation, Funding acquisition, Supervision, Writing – review & editing.

Declaration of competing interest

The authors declare that they have no known competing financial interests or personal relationships that could have appeared to influence the work reported in this paper.

Acknowledgements

The authors acknowledge the financial support of COWI Foundation, Denmark and VSL International, Switzerland and the technical support of FORCE Technology.

Role of the funding source

None of the sponsors were involved in the study design; in the collection, analysis and interpretation of data; in the writing of the report; and in the decision to submit the article for publication.

References

Aydin, T.B., Joshi, A., Ekmekci, A., 2014. Critical effects of a spanwise surface wire on flow past a circular cylinder and the significance of the wire size and Reynolds number. J. Fluids Struct. 51, 132–147. http://dx.doi.org/10.1016/j.jfluidstructs.2014.08.006.

Burlina, C., Georgakis, C.T., Larsen, S.V., Egger, P., 2018. Aerodynamics and rain rivulet suppression of bridge cables with concave fillets. Wind Struct. 26 (4), 253–266. http://dx.doi.org/10.12989/was.2018.26.4.253.

Cooper, K.R., Mercker, E., Wiedemann, J., 1999. Improved blockage corrections for bluff bodies in closed and open wind tunnels. In: Larsen, A., Larose, G., Livesey, F. (Eds.), Wind Engineering Into the 21st Century. CRC Press / Balkema, Rotterdam, Netherlands, pp. 1627–1634.

Georgakis, C.T., Koss, H.H., Ricciardelli, F., 2009. Design specifications for a novel climatic wind tunnel for the testing of structural cables. In: The 8th International Symposium on Cable Dynamics. Paris, France.

Keefe, R.T., 1962. Investigation of the fluctuating forces acting on a stationary circular cylinder in a subsonic stream and of the associated sound field. J. Acoust. Soc. Am. 34 (11), 1711–1714. http://dx.doi.org/10.1121/1.1909102.

Kleissl, K., 2013. Cable Aerodynamic Control - Wind Tunnel Studies (Ph.D. thesis). Technical University of Denmark, Kgs. Lyngby, Denmark.

Kleissl, K., Georgakis, C.T., 2012. Comparison of the aerodynamics of bridge cables with helical fillets and a pattern-indented surface. J. Wind Eng. Ind. Aerodyn. 104–106, 166–175. http://dx.doi.org/10.1016/j.jweia.2012.02.031.

Macdonald, J.H.G., Larose, G.L., 2006. A unified approach to aerodynamic damping and drag/lift instabilities, and its application to dry inclined cable galloping. J. Fluids Struct. 22 (2), 229–252. http://dx.doi.org/10.1016/j.jfluidstructs.2005.10.002.

Matejicka, L., Georgakis, C.T., Koss, H.H., Egger, P., 2021. Ice-shedding and aerodynamic investigations of bridge cables with steel wire meshes. In: Abu, A. (Ed.), Proceedings of IABSE Congress, Resilient Technologies for Sustainable Infrastructures. IABSE, Zurich, Switzerland, pp. 94–102.

Matejicka, L., Georgakis, C.T., Schwarz, A., Egger, P., 2019. Cable surface for the reduction of risk associated with bridge cable ice accretions. Struct. Eng. Int. 29 (3), 425–432. http://dx.doi.org/10.1080/10168664.2019.1597453.

Matteoni, G., Georgakis, C.T., 2012. Effects of bridge cable surface roughness and cross-sectional distortion on aerodynamic force coefficients. J. Wind Eng. Ind. Aerodyn. 104–106, 176–187. http://dx.doi.org/10.1016/j.jweia.2012.02.029.

Nims, D.K., Hunt, V.J., Helmicki, A.J., Ng, T.T., 2014. Ice Prevention or Removal on the Veteran's Glass City Skyway Cables. Final Report FHWA/OH-2014/11, University of Toledo, Toledo, OH.

Norberg, C., 2003. Fluctuating lift on a circular cylinder: review and new measurements. J. Fluids Struct. 17 (1), 57–96. http://dx.doi.org/10.1016/S0889-9746(02)00099-3.

Schewe, G., 1983. On the force fluctuations acting on a circular cylinder in crossflow from subcritical up to transcritical Reynolds numbers. J. Fluid Mech. 133, 265–285. http://dx.doi.org/10.1017/S0022112083001913.

Zdravkovich, M.M., 1997. Flow Around Circular Cylinders Vol 1: Fundamentals. Oxford University Press, New York.